



HAL
open science

Characterization and limits of a cold atom Sagnac interferometer

Alexandre Gauguet, Benjamin Canuel, Thomas Lévêque, Walid Chaibi,
Arnaud Landragin

► **To cite this version:**

Alexandre Gauguet, Benjamin Canuel, Thomas Lévêque, Walid Chaibi, Arnaud Landragin. Characterization and limits of a cold atom Sagnac interferometer. 2009. hal-00403630v2

HAL Id: hal-00403630

<https://hal.science/hal-00403630v2>

Preprint submitted on 20 Jul 2009 (v2), last revised 17 Nov 2009 (v3)

HAL is a multi-disciplinary open access archive for the deposit and dissemination of scientific research documents, whether they are published or not. The documents may come from teaching and research institutions in France or abroad, or from public or private research centers.

L'archive ouverte pluridisciplinaire **HAL**, est destinée au dépôt et à la diffusion de documents scientifiques de niveau recherche, publiés ou non, émanant des établissements d'enseignement et de recherche français ou étrangers, des laboratoires publics ou privés.

Characterization and limits of a cold atom Sagnac interferometer

A. Gauguet*, B. Canuel†, T. Lévêque, W. Chaibi‡, and A. Landragin§

LNE-SYRTE, UMR 8630 CNRS, UPMC, Observatoire de Paris,

61 avenue de l'Observatoire 75014 Paris, FRANCE

(Dated: July 20, 2009)

We present the full evaluation of a cold atom gyroscope based on atom interferometry. We have performed extensive studies to determine the systematic errors, scale factor and sensitivity. We demonstrate that the acceleration noise can be efficiently removed from the rotation signal allowing to reach the fundamental limit of the quantum projection noise for short term measurements. The technical limits to the long term sensitivity and accuracy have been identified, clearing the way for the next generations of ultra-sensitive atom gyroscopes.

PACS numbers: 03.75.Dg, 06.30.Gv, 37.25.+k, 67.85.-d

I. INTRODUCTION

Inertial sensors are of interest in both science and industry. Higher precision sensors could find scientific applications in the areas of general relativity [1], geophysics [2] and in the field of navigation [3]. In these fields, matter-wave interferometry is promising since it is expected to be an extremely sensitive probe for inertial forces [4]. In 1991, atom interferometry techniques have been used in proof-of-principle works to measure rotations [5] and accelerations [6]. First demonstrations of highly sensitive atomic gyroscopes using thermal beams [7, 8] were obtained in 1997 and then followed by the achievement of sensors with sensitivities at the state-of-the-art level [9, 10]. For practical applications, cold atom interferometry should be of main interest thanks to its intrinsic stability and accuracy, as the measurement of the inertial forces is realized with respect to the inertial frame of the free-falling atoms. The use of cold atoms allows a better control of atomic velocity and interaction time, leading to a better accuracy in a much more compact gyroscope [11, 12, 13, 14].

In this paper we present the full characterization of a gyroscope based on atom interferometry, sensitive to the Sagnac effect. Different parameters have been taken into account for the study: the short term noise, the stability of the systematics, the scale factor and its linearity. The apparatus uses Cesium atoms and Raman transition to manipulate the matter wave-packets. In our setup, we use a single Raman beam interacting with slow atoms, which make the setup very versatile. Thus, the experiment enables to measure the full base of inertia (three components of acceleration and rotation) on the same

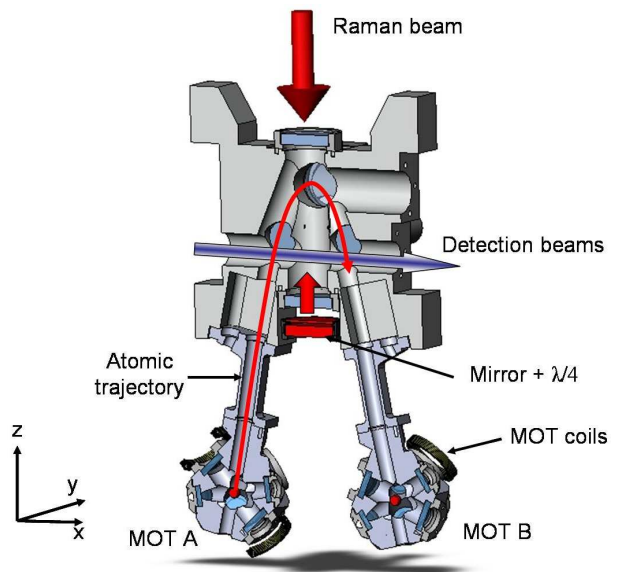


FIG. 1: Scheme of the vacuum chamber showing the two MOTs, the interferometer zone and detection probe. The total dimensions of the system is 30 x 10 x 50 cm.

apparatus [11], which is suitable for applications as in inertial navigation. In this paper, we emphasize on the possibility to measure the systematics and the scale factor accurately thanks to this polyvalent apparatus. In section II, we first describe the experimental setup and the measurement process. A detailed analysis of the different sources of systematics and tests of the scaling factor are presented in section III. Finally, the analysis of the stability of the rotation measurement and its main limits are described in section IV.

II. APPARATUS

A global view of the experimental setup is presented in Fig. 1. The whole experiment is surrounded by two layers of mu-metal shield, so as to reduce the impact of external magnetic fields. Cesium atoms are first loaded from

*Present address: Department of Physics, Durham University, Rochester Building, South Road, Durham DH1 3LE, England

†Present address: European Gravitational Observatory, Via E. Amaldi, 56021 S. Stefano a Macerata - Cascina (PI), Italy

‡Present address: ARTEMIS - Observatoire de Nice, Boulevard de l'Observatoire, 06305 Nice, France

§arnaud.landragin@obspm.fr; LNE-SYRTE, UMR 8630 CNRS, UPMC, Observatoire de Paris

a vapor into two independent Magneto-Optical Traps (MOT), called A and B in the following. The two Cesium clouds are then launched into two opposite parabolic trajectories using moving molasses technique. At the top of their trajectory, atoms interact successively three times with a unique pair of retro-reflected Raman beams, which acts on matter-waves as beam splitters or mirrors, and create an interferometer of 80 ms total maximum interaction time. The atomic phase shift is then worked out from the population in each output port, which is measured by a fluorescence technique thanks to the state labelling of the interferometer output ports [15].

In this paper, we will focus on the configuration based on vertical Raman beams. The use of two atomic sources allows to discriminate between the acceleration along the vertical direction and the rotation around the y horizontal axis. The setup is fixed on a rotation stage, vertically oriented which enables to vary the projection of the Earth's rotation rate along the sensitive axis of the gyroscope.

A. Atomic preparation

Cesium atoms are first loaded from a thermal vapor during 140 ms into two independent MOTs. After the MOT-coils are turned off, the atoms are kept in an optical molasses for 15 ms, waiting for the decrease of the stray magnetic field. Then, a frequency shift between the upper and the lower cooling beams is applied to launch the atoms thanks to the moving molasses technique. The independent control of the lower and upper cooling beams frequencies is achieved by passing through two different acousto-optic modulators (AOM). By applying a frequency shift of 3.2 MHz on the AOM controlling the lower cooling beams, atoms are launched at a velocity of 2.4 m.s^{-1} with an angle of 8° with respect to the vertical direction. In addition, the atoms are cooled down to a temperature of about $1.2 \mu\text{K}$ in the molasses by chirping the mean frequency down to -15Γ , with respect to the closed transition $|F=4\rangle \leftrightarrow |F'=5\rangle$.

Following this launching stage, the atoms are distributed among all Zeeman sub-levels of the $|6S^{1/2}, F=4\rangle$ state. In order to reduce the sensitivity to parasitic magnetic fields, atoms are selected in the sub-level $m_F=0$. For this purpose, a static magnetic field of 30 mG is applied in the z direction to lift the degeneracy of the Zeeman sub-levels. Atoms in $|6S^{1/2}, F=4, m_F=0\rangle$ are transferred to $|6S^{1/2}, F=3, m_F=0\rangle$ when passing through a microwave cavity. Atoms remaining in $|6S^{1/2}, F=4\rangle$ are then removed by means of a pusher beam. After this preparation stage, we obtain typically 10^7 atoms in the $|6S^{1/2}, F=3, m_F=0\rangle$ ground state with a residual in the other states of less than 1% for both sources.

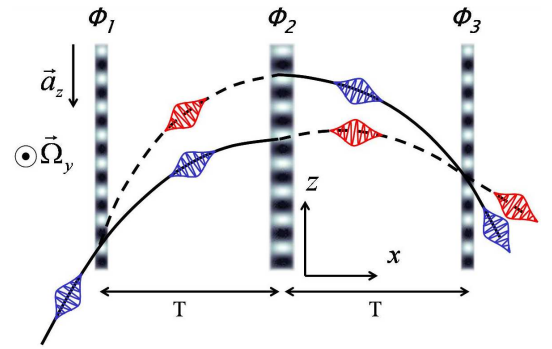


FIG. 2: Scheme of the $\pi/2 - \pi - \pi/2$ interferometer in the vertical Raman configuration with a total interaction time of $2T$. The interferometer is sensitive to the vertical acceleration a_z , the rotation Ω_y . Solid and dotted lines respectively represent the partial wave packets in the state $|6S_{1/2}, F=3\rangle$ and $|6S_{1/2}, F=4\rangle$.

B. Implementation of the interferometer

1. Three pulses interferometer

When the atoms arrive close to the apex of the parabolic trajectories, occurring at $t_{ap} = 244 \text{ ms}$ after the launching, the wave packets are split, deflected and recombined with stimulated Raman transitions [6], in order to realize the interferometer. Since the Raman beams are vertically oriented the interferometric area is created in the (x,z) plane (Fig. 2).

The output phase shifts of both interferometers $\Delta\Phi^{A,B}$ are composed of three terms which respectively depend on the acceleration \mathbf{a} , the rotation Ω and the Raman laser phase difference at the moment of each pulses Φ_i [16]:

$$\Delta\Phi^{A,B} = \Delta\Phi_a + \Delta\Phi_{\Omega}^{A,B} + \Delta\Phi_{laser} \quad (1)$$

In the vertical Raman configuration studied here, these contributions are written as a function of the vertical acceleration a_z , the horizontal rotation Ω_y and the Raman laser phase shift ϕ_i :

$$\begin{aligned} \Delta\Phi_a &= k_{\text{eff}} a_z T^2 \\ \Delta\Phi_{\Omega}^{A,B} &= 2 k_{\text{eff}} V_x^{A,B} \Omega_y T^2 \\ \Delta\Phi_{laser} &= \phi_1 - 2\phi_2 + \phi_3 \end{aligned} \quad (2)$$

where \mathbf{k}_{eff} is the effective wave-vector of the Raman beam. The rotation phase shifts $\Delta\Phi_{\Omega}^{A,B}$ measured by each interferometer are related to the horizontal velocities $V_x^{A,B}$ and have opposite signs for the two sources. The use of two contra-propagating sources allows to discriminate between acceleration and rotation phase shifts [9].

2. Raman lasers

In order to drive Raman transitions between $|6S_{1/2}, F = 3, m_F = 0\rangle$ and $|6S_{1/2}, F = 4, m_F = 0\rangle$, two contra-propagating laser beams, with a frequency difference of 9.192 GHz, are required. These two optical frequencies are generated by two extended cavity laser diodes [17] emitting at $\lambda = 852$ nm. The first laser is locked by frequency comparison to the MOT repumper beam with a detuning of 350 MHz with respect to the $|6S_{1/2}, F = 3, m_F = 0\rangle \leftrightarrow |6P_{3/2}\rangle$ transition. A second laser is phase-locked onto the previous one by comparing the beat note between the two beams with a microwave reference [18]. In order to get sufficient power to drive the transitions, the two laser beams are injected in a common semiconductor tapered amplifier (EYP-TPA-0850-01000-3006-CMT03) [19]. The power ratio between the two lasers is adjusted close to 0.5 in order to cancel the effect of the AC Stark shift (see part III C 2). This ratio is then finely tuned by means of Raman spectroscopy on the cold atom samples. After amplification, the two lasers have the same polarization and are guided to the atoms through the same polarizing fibre. At the output of the fiber, the beam is collimated with an achromatic doublet lens of 240 mm focal length, giving a diameter at $1/e^2$ of 35 mm. The intensity at the center of the beam is 20 mW.cm^{-2} . The two contra-propagating beams are obtained thanks to a retro-reflected configuration in which the two frequency beam passes through the vacuum chamber and is reflected by a mirror, crossing a quarter-wave plate twice (Fig. 1). The wave plate is set in such a way that retro-reflected polarizations are orthogonal with respect to the incident ones. In this manner, counter-propagating Raman transitions are allowed while co-propagating ones are forbidden. This retro-reflected configuration limits the parasitic effects induced by the wave-front distortions, which are critical to achieve a good accuracy and long term stability (see part III C 4).

Moreover, since the atoms are in free fall, the frequency difference between the two atomic levels is Doppler shifted in the vertical direction by $\omega_D = \mathbf{k}_{\text{eff}} \cdot \mathbf{g}(t - t_{\text{ap}})$ according to the gravity g . In order to satisfy the resonance condition during all the atomic flight, the frequency difference between the two Raman lasers is chirped thanks to a Direct Digital Synthesizer (DDS). Additionally the interferometers are realized with a delay of 5 ms with respect to the apex of the trajectories in order to avoid a null Doppler shift during the π pulse.

C. Detection system

1. Detection apparatus

With Raman transitions, state labelling [15] enables to determine the momentum state of the atoms by measuring their internal state. Thus, the phase shift of the interferometer can be simply obtained by

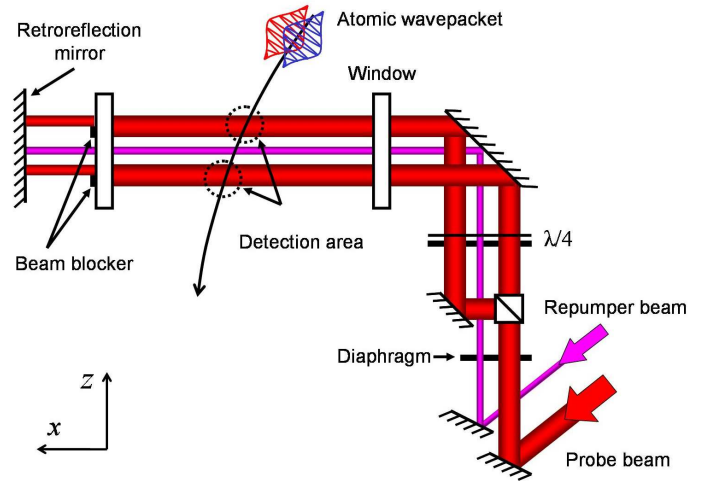


FIG. 3: Scheme of the detection system. Two retro-reflected probe beams are generated from the same laser while a repumper beam is inserted between the two. These three beams are shaped to form horizontal slices thanks to two slits.

measuring the transition probability of the atoms between the two ground states $|6S_{1/2}, F = 3, m_F = 0\rangle$ and $|6S_{1/2}, F = 4, m_F = 0\rangle$ at the output of the interferometer. The population measurement is then performed by counting the number of fluorescence photons emitted by each ground state at the crossing of successive laser beams. These beams are shaped to form horizontal slices of light with a rectangular section of 10×5 mm so as to probe the whole atomic clouds.

The detection system is made up of three counter-propagating beams circularly polarized as shown in Fig. 3. Upper and lower beams are used as probes with a saturation parameter of 0.3. They are obtained from the same laser, tuned on the closed atomic transition $|6S_{1/2}, F = 4\rangle \leftrightarrow |6P_{3/2}, F' = 5\rangle$. A repumper beam is inserted between these two probes and tuned on the transition $|6S_{1/2}, F = 3\rangle \leftrightarrow |6P_{3/2}, F' = 4\rangle$.

After the interferometric sequence, the atoms pass through the first probe. The fluorescence light emitted by the atoms in the $|6S_{1/2}, F = 4\rangle$ state is collected by an imaging system (3.7 % efficiency) and focused onto a photodiode (Hamamatsu 1327BQ). The output signal s_1 , given by the area of the time-of-flight signal, is proportional to the number of atoms projected in the $|6S_{1/2}, F = 4\rangle$ state. The lower part of this first probe beam is not retro-reflected in order to blow away these atoms. The remaining cloud, made up of atoms in the $|6S_{1/2}, F = 3\rangle$ ground state, is optically pumped to the $|6S_{1/2}, F = 4\rangle$ state passing through the repumper beam. These atoms are finally detected with the second probe beam providing a signal s_2 proportional to the number of atoms initially in the state $|6S_{1/2}, F = 3\rangle$ at the output of the interferometer. Each interferometer uses two imaging systems in order to collect the signal emitted by the atoms in the two respective ground states. The

transition probability P is deduced from the fluorescence signals obtained on the two photodiodes (s_1 and s_2) and written: $P = \frac{s_1}{s_1 + s_2}$.

2. Detection noise analysis

The noise affecting the fluorescence signals can be separated into three main contributions [20]. The first one is related to power or frequency fluctuations of the probe beams that induce a noise which scales linearly with the total number of atoms in each source $N^{A,B}$. The second contribution consists in a technical noise linked to the detection system (photodiode dark current and amplifier noise) that gives a contribution independent of the total number of atoms in the probe. Finally, the quantum projection noise (QPN) gives a fundamental limit of the measurement [21] and scales as $(P^{A,B}(1 - P^{A,B})N^{A,B})^{1/2}$. These independent sources of noise can be quadratically added, giving a variance of the transition probability:

$$\sigma_{P^{A,B}}^2 = \alpha + \frac{P^{A,B}(1 - P^{A,B})}{N^{A,B}} + \frac{\gamma}{N^{A,B}^2} \quad (3)$$

In order to determine the parameters α and γ when working at a side of fringe of the interferometer, we use a single Raman laser pulse leading to an average transition probability close to 0.5. In such a case, the noise detection properties are similar to these of the interferometer without being sensitive to its own phase noise. In practice, the Raman laser power is reduced so that the Raman pulse duration $\tau = \pi/\Omega_{Rabi}$ limits the average transition probability to $P^{A,B} = 0.5$ by velocity selection. By this mean, the measurement remains almost insensitive to potential power fluctuations of the Raman beam.

Noise	measures
Laser	$a = \sqrt{\alpha} = 4 \cdot 10^{-4}$
QPN	$b = 1/(2\sqrt{\eta}) = 7 \cdot 10^{-2}$
Technical	$c = \sqrt{\gamma}/\eta = 1.6$

TABLE I: Table of the fitting parameters deduced from the measurement of the detection noise, presented in Fig. 4.

The detection noise σ_P is evaluated as a function of the number of detected atoms, changed by varying the loading time of the MOTs (see Fig. 4). The data are scaled as a function of the fluorescence signal $S = s_1 + s_2$, which is proportional to the actual atom number $N^{A,B} = \eta S$. The two detection systems clearly show identical noises for the two atomic sources. A fit of the experimental data has been realized by eq. 3 in which the scaling of the number of atoms is a free parameter. This leads to a fit with three parameters (a , b , c), related to α , γ and η , which are reported in Table I. For the usual experimental parameters, the number of detected atoms corresponds to $S = 7000$ and the signal to noise is then limited by

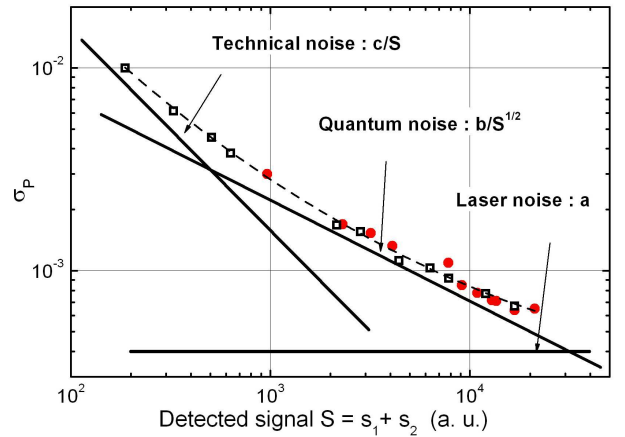


FIG. 4: Detection noise analysis. The shot-to-shot Allan standard deviation of the transition probability is plotted versus the detected signal S in the same arbitrary unit for the two sources (respectively black squares and red dots). The dash curve corresponds to the fit of the data by the noise model, which can be separated in three terms corresponding to the three lines.

the quantum detection noise. In this case, the parameter b enables to determine the actual number of atom detected for each sources $N = 3.6 \times 10^5$ atoms, which is in agreement with additional measurements realized by absorption.

D. Measurement process

Interference fringe patterns are scanned by taking advantage of the Raman laser phase control. Indeed, by adding a laser phase offset $\delta\varphi_n$ between the second and the third pulse of the n^{th} measurement, the atomic phase measured evolves as $\Delta\Phi_{laser} = \phi_1 - 2\phi_2 + (\phi_3 + \delta\varphi_n)$. In practice, the phase increment $\delta\varphi_n$ is applied to the micro-wave signal used as a reference to phase-lock the two Raman lasers. The fringe patterns, shown in the Fig. 5, were obtained with the usual parameters, e.g. $2T = 80$ ms and Raman pulse durations of $\tau = 13 \mu s$. Both atomic sources exhibit a contrast C close to 30% mainly limited by the Raman transition efficiency. Two phenomena are responsible for this limitation. In one hand, the atomic cloud velocity distribution is broader than the velocity linewidth of the Raman transition. In the other hand, because of the thermal expansion of the atomic cloud, all the atoms do not experience the same laser power in the gaussian Raman beam, and therefore do not experience the same Rabi frequency.

The transition probability measured at the output of the interferometer is written as a function of the following terms: an offset $M^{A,B}$, a contrast $C^{A,B}$, a phase shift due to inertial effects $\Delta\Phi_I^{A,B}$ (acceleration and rotation) and

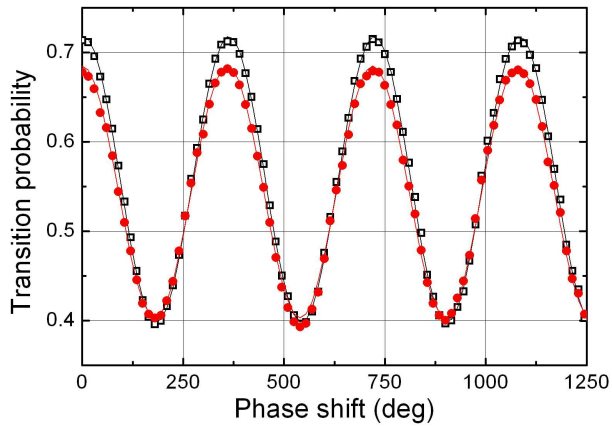


FIG. 5: Atomic fringe patterns obtained for the both interferometer A (black squares) and B (red dots) with an interaction time of $2T = 80$ ms and a pulse duration of $13 \mu\text{s}$. In order to scan the fringe patterns we incremented the effective Raman laser phase at each measurement cycle.

a laser phase shift $\Delta\Phi_{laser}$:

$$\begin{aligned} P^A &= M^A + C^A \cos(\Delta\Phi_I^A + \Delta\Phi_{laser}) \\ P^B &= M^B + C^B \cos(\Delta\Phi_I^B + \Delta\Phi_{laser}) \end{aligned} \quad (4)$$

The phase shift accumulated by the two interferometers can then be deduced by fitting each fringe pattern with the equation $P^{A,B} = M^{A,B} + C^{A,B} \cos(\Delta\Phi^{A,B} + \Delta\Phi_{laser})$, where $\Delta\Phi^{A,B}$ is the unknown phase and $\Delta\Phi_{laser}$ the laser phase offset added to scan the fringes. Acceleration and rotation phase shifts are then discriminated by realizing respectively the half sum and half difference of the two fitted phase shifts:

$$\Delta\Phi_a = \frac{\Delta\Phi^A + \Delta\Phi^B}{2} \quad \Delta\Phi_\Omega = \frac{\Delta\Phi^A - \Delta\Phi^B}{2} \quad (5)$$

In the general case, the interferometric phase shift can always be extracted from four points: $\Delta\Phi_{laser} = 0^\circ, +90^\circ, +180^\circ$ and 270° .

With the retro-reflected configuration, atoms are submitted to four laser waves which couple Raman transitions along two opposite effective wave-vectors $\pm\mathbf{k}_{eff}$. The opposite Doppler shift between these two effective transitions allows to deflect the atomic wave packets along one or the other direction by changing the sign of the frequency ramp delivered by the DDS. The sign of the inertial phase shifts $\Delta\Phi_I^{A,B}$ changes according to $\pm\mathbf{k}_{eff}$. Consequently, by processing the half difference of the phase shift measured at $\pm\mathbf{k}_{eff}$, parasitic phase shifts independent on the direction of the effective wave vector are removed thanks to this k-reversal technique.

To sum up, the experimental sequence consists in acquiring transition probability measurements on the two sources, alternately for each direction of the wave vector $\pm\mathbf{k}_{eff}$. The fit is processed afterwards and we infer a measurement of the inertial phase shifts for each set of eight acquisition points.

III. SYSTEMATIC ERRORS AND SCALE FACTOR

A. Characterization of the atomic trajectories

A crucial point, when measuring a differential phase shift between two interferometers [9, 22, 23], is the overlap of both atomic trajectories. Indeed, if the trajectories are perfectly overlapped, many systematic effects cancel out, as explained in paragraph III C. Consequently, the two cold atom sources were realized with a particular care. In this section, we study both overlap and stability of the two trajectories.

1. Overlap of the atomic trajectories

When using Raman laser beams oriented in the vertical direction, the atomic trajectories have to be overlapped in the orthogonal plane (xy) since the Raman laser system remains invariant along the z direction. In addition, the two atomic clouds must be resonant simultaneously with the single Raman beams which implies that vertical velocities must be equal. The key parameters allowing to fulfill these requirements are the initial positions and velocities of the two atomic sources. Despite a careful alignment and power adjustment of the twelve trap laser beams, the overlap of the two trajectories has to be finely tuned. The adjustment of velocities is achieved by modifying the launching directions (thanks to the tilt of the experiment) and by changing independently the values of launching velocities. The relative positions at the moment of the Raman pulses have been optimized by adjusting the timing sequence and the position of the zeros of the quadratic magnetic fields in the two traps.

We directly map the two trajectories in the interferometer zone thanks to the Raman laser beams, with a movable aperture of diameter of 5 mm. By maximizing the transfer efficiency of a Raman pulse, we deduce the actual position of each atomic cloud in the xy plan at a given time. The Fig. 6 presents the two trajectories which are overlapped to better than 0.5 mm over the whole interferometer zone. The measurement resolution is limited by the spatial extension of the atomic clouds (5 mm FWHM at the apex).

2. Stability of the trajectory overlap

The stability of the overlap is of first interest in the stability of the rotation rate measurements (paragraph IV). Ideally, independent measurements of the initial velocities and positions of the two sources in the (xy) plan should be performed. Unfortunately, the use of the time of flight method and Raman lasers along either the y or the z axes only gives access to the initial positions stabilities in the z axis and velocities in the y and z directions. Nevertheless, this measurement gives an evaluation of the

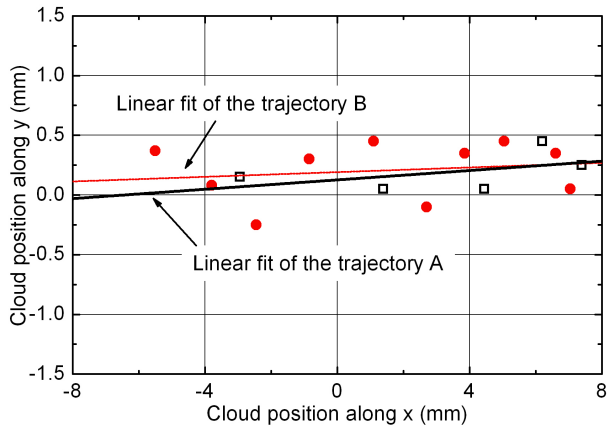


FIG. 6: Trajectories of the atomic cloud A (black squares) and B (red dots) in the xy plan, in the interaction area. Two linear fits of experimental data show that the overlap is better than 0.5 mm, limited by the measurement resolution.

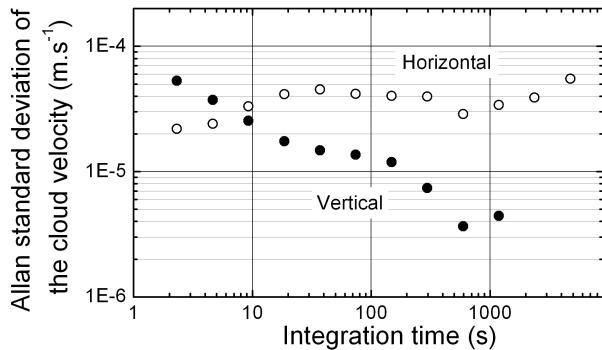


FIG. 7: Allan standard deviation of the atomic velocity for the source A measured by Raman spectroscopy. The analysis is carried out from a 12 hours continuous acquisition.

typical fluctuations of position and velocity which are needed in the analysis of the long term stability.

The atomic velocity stability is measured by Raman spectroscopy, using horizontal or vertical Raman laser beams. For counter-propagating Raman beams, the resonance condition depends on the Doppler effect and leads to a measurement of the atomic velocity. In addition, to discriminate the Doppler effect from other sources of frequency shift, we use the k-reversal method described in chapter II D. Fig. 7 shows the standard Allan deviations of velocities along the z and y directions for source A. Similar behaviors have been recorded for source B, with stabilities comprised between 2 and 30 $\mu\text{m.s}^{-1}$ for time scale from 1 to 5000 s. In addition, the fluctuations of the initial position along the vertical direction can be worked out by combining the previous velocity data with simultaneous time of flight measurements. Therefore we can estimate the Allan standard deviation of the initial position, which is 28 μm at 2 seconds, averaging for the long times (1000 s) to reach 15 μm . Combining these positions and velocities fluctuations independently, we in-

fer a typical overlap fluctuation around 20 to 30 μm in the interferometer zone. In order to explain the sources of these fluctuations, additional studies have been performed. They demonstrate that relative power and polarization fluctuations of the opposite cooling beams can explain this result. Indeed, we measured a change of the launching velocity of 36 $\mu\text{m.s}^{-1}$ for 1% of polarization fluctuation and a initial displacement of 50 μm for 1% of intensity fluctuation between the three top and the three bottom cooling beams [24]. In the usual operation, the polarization fluctuations are the dominant effect which affects the stability of the trajectories.

B. Measurement of the systematic errors and the scale factor

In order to perform inertial force measurements, we need to know accurately the scale factor and the systematic errors, which link the actual rotation and acceleration quantities to the measured phase shifts $\Delta\Phi_{\text{rot}}$ and $\Delta\Phi_{\text{acc}}$. In order to determine these two parameters for rotation, we change, in a controlled way, the rotation rate measured by the gyroscope. In addition, taking advantage of the single Raman laser beam pair, the interaction time T can be changed continuously from $T = 0$ to 40 ms. The systematic errors and scale factor measurement were performed for various interaction time, giving a test of the quadratic scaling of the rotation phase shift with T .

1. Dependence with the rotation rate

The first test of the rotation scale factor consists in checking the proportionality between the rotation phase shift and the rotation rate. For this purpose, the orientation θ , between the sensitive axis of the gyroscope and the East-West direction, is changed to measure different horizontal projections of the Earth rotation rate $\Omega_y = \Omega_h \sin \theta$. At the Observatoire de Paris, located at the latitude $\lambda = 48^\circ 50' 08''$, the horizontal rotation rate Ω_h is $4.8 \times 10^{-5} \text{ rad.s}^{-1}$. The whole device is placed on a rotation mount, which determines the orientation with a relative accuracy of 50 μrad .

In Fig. 8 the rotation phase shift is plotted with respect to the orientation of the gyroscope. The experimental data are fitted by a sinusoidal function $\Delta\Phi = \Delta\Phi_{\Omega}^{er} + A^{(0)} \sin(\theta - \theta_0)$. The magnitude $A^{(0)}$ is used to calibrate the rotation scale factor: we find $A^{(0)} / (\Omega_T \sin \lambda) = 15124 \pm 12 \text{ rad/rad.s}^{-1}$. Moreover this measurement allows to deduce the systematic error on the rotation signal: $\Delta\Phi_{\Omega}^{er} = 28.3 \pm 0.7 \text{ mrad}$.

The same data, when plotted as a function of the actual rotation rate, are well aligned with a slope equal to the scale factor. Non-linearities appear as deviations to the perfect straight line and can be evaluated by fitting with

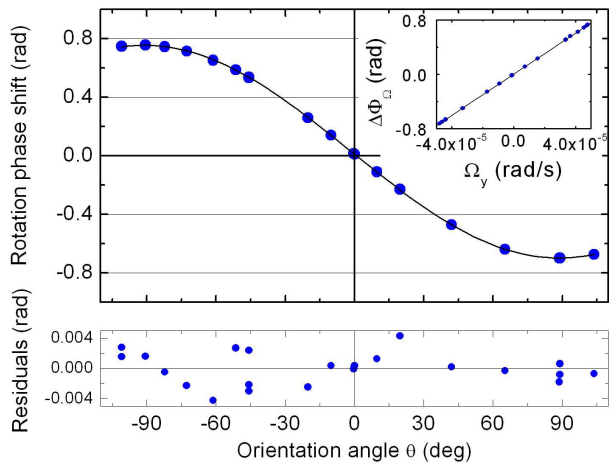


FIG. 8: Measurement of the rotation phase shift as a function of the orientation θ of the experimental setup with respect to the East-West direction. Experimental data (dots) and their sinusoidal fit (line) are displayed on the top graph while their residuals are shown at the bottom. The inset exhibits the same data reported as a function of the actual rotation rate. The residuals

a quadratic term. Their relative contributions are below 10^{-5} in the range of measurement.

2. T scaling of the rotation phase shift

In order to test the T^2 scale factor dependance, the experimental setup is orientated at $\theta \simeq \pm 90^\circ$ for which the sensitivity of the gyroscope to the Earth rotation is maximum. We also take advantage of the fact that, for these two orientations, an error in the orientation angle θ has a second order effect on the rotation phase shift. Therefore we write:

$$\begin{aligned} \Delta\Phi_{\Omega}^{+90^\circ}(T) &= \Phi_{rot}^{er}(T) - 2k_{\text{eff}}V_x\Omega_yT^2 \\ \Delta\Phi_{\Omega}^{-90^\circ}(T) &= \Phi_{rot}^{er}(T) + 2k_{\text{eff}}V_x\Omega_yT^2 \end{aligned} \quad (6)$$

where $\Phi_{rot}^{er}(T)$ is the systematic error on the rotation signal for a given interaction time T . The half difference of the signal measured at $\theta = +90^\circ$ and $\theta = -90^\circ$ (Fig. 9(a)) gives a test of the scaling of the rotation phase shift as T^2 . It shows an excellent agreement with the expected behavior. In addition, the systematic error which impact the rotation signal is deduced from the half sum of the signals for the both orientations. The evolution of the error phase shift is displayed as a function of the interaction time in Fig. 9(b). Negligible for small interaction time, it increases up to 34 mrad. For the usual interaction time of $2T = 80$ ms, this systematic error reaches 28.3 mrad. The study of the different sources of systematic errors is performed in the following section.

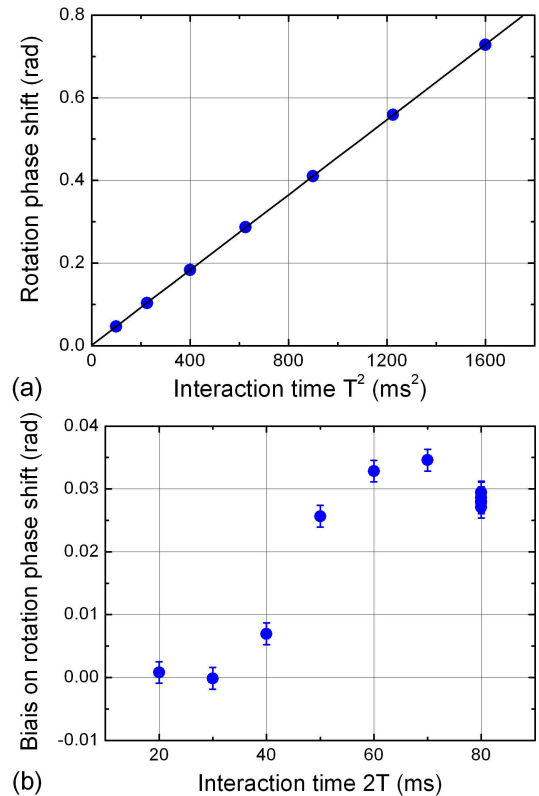


FIG. 9: (a) Evaluation of the actual rotation phase shift versus the interaction time T^2 . In this figure the systematic error is cancelled with the subtraction of the rotation signals obtained at $\pm 90^\circ$. (b) Systematic error on the rotation signal as a function of the interaction time $2T$. The systematic error is evaluated by making the half sum of the rotation signal measured at $\pm 90^\circ$.

C. Investigation of the sources of systematic errors

1. Quadratic Zeeman effect

The first expected source of systematic error in the interferometer phase shift comes from the Zeeman shift induced by the magnetic field. In order to limit its impact, the interferometer is realized between the two $m_F = 0$ Zeeman sub-levels, whose difference of energy evolves quadratically with the magnetic field as: $\Delta_{mag} = K^{(2)}B^2$ ($K^{(2)} = 427.45 \text{ Hz}\cdot\text{G}^{-2}$ for Cesium atoms). In addition, thanks to the symmetric features of the interferometer, the phase shift is not sensitive to a constant frequency shift. However, a magnetic field gradient breaks the symmetry and gives rise to a phase shift. Assuming a linear gradient δ_{bx} along the atomic trajectories the phase shift induced is:

$$\Delta\Phi_{mag} = -4\pi K^{(2)}B_0T^2V_x\delta_{bx} \quad (7)$$

Both MOTs and the interaction region are set into three independent magnetic shields and the whole experiment is inside a second layer of shield so as to limit

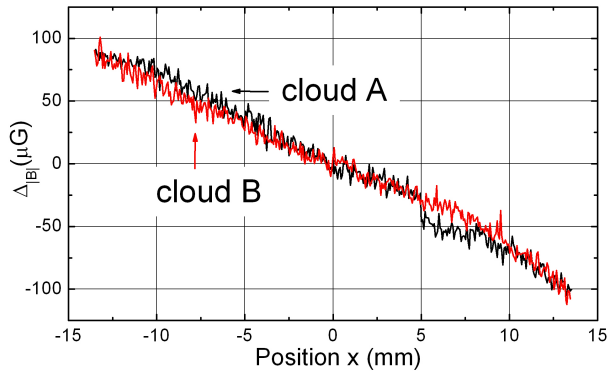


FIG. 10: Measurement of the magnetic field as a function of the position of the atoms along their trajectory in the interaction zone.

the influence of the ambient magnetic field. The magnitude of the residual magnetic field has been measured by selecting the atoms in the $m_F = 2$ sub-level and driving magnetic transitions thanks to a microwave antenna. By measuring the frequency of the transition between the $|6S_{1/2}, F = 3, m_F = 2\rangle$ and $|6S_{1/2}, F' = 4, m_{F'} = 2\rangle$ states along the trajectories, we mapped the value of the magnetic field in the interaction zone. The results of these measurements are displayed in Fig. 10 for the two atomic clouds. We measured a gradient of $\delta_{bx} = 7 \text{ mG}\cdot\text{m}^{-1}$ giving a small phase shift on the rotation signal of 0.6 mrad. This Zeeman phase shift does not depend on the laser wave vectors, therefore it cancels out with the k-reversal technique and so disappears on the total interferometer phase shift.

2. AC Stark shift

We study the effect of a frequency shift induced by the AC Stark shift Δ_{AC} on the interferometer phase shift [25]. This frequency shift between the two hyperfine levels can be cancelled by setting a proper intensity ratio between the two Raman beams. However, if the ratio is flawed, a phase shift $\Delta\Phi_{AC}$ is induced on the interferometer. Assuming the AC Stark shift constant during each laser pulse, it yields:

$$\Delta\Phi_{AC} = \left(\frac{\Delta_{AC}^{(3)}}{\Omega_{\text{eff}}^{(3)}} - \frac{\Delta_{AC}^{(1)}}{\Omega_{\text{eff}}^{(1)}} \right) \quad (8)$$

where $\Delta_{AC}^{(1,3)}$ are the frequency shifts of the Raman transition at the time of the first and the third pulse, and $\Omega_{\text{eff}}^{(1,3)}$ are the respective effective Rabi frequencies [26]. In our experimental setup, the two Raman lasers are provided by a single optical fiber and retro-reflected, insuring the stability of the intensity ratio between the two lasers throughout the Raman beam.

The equation (8) shows that if the atomic trajectories are perfectly overlapped and symmetric with respect to

the center of the Raman beam, the phase shift $\Delta\Phi_{AC}$ remains equal to zero as the contributions of the first and last pulse are identical. By opposition, a parasitic phase shift appears on the acceleration signal if the gaussian profile of the Raman beam is not centered with respect to the three pulse sequence of the interferometer. A similar effect would be induced by time fluctuations of the laser power at the output of the fiber. Moreover, this phase shift also affect the rotation signal if the two trajectories are not perfectly superimposed.

The sensitivity of the rotation signal to the AC Stark shift was characterized by changing the intensity ratio between the two Raman lasers so as to induce a frequency shift of $\Delta_{AC} = 10 \text{ kHz}$. A sensitivity of 5 mrad/kHz was measured. This AC Stark shift is however independent on the effective wave vector \mathbf{k}_{eff} , then it can be rejected by the k-reversal method considering that the fluctuation of $\Delta\Phi_{AC}$ is slow enough compared with the repetition rate of the measurement. Using this technique, we measure a residual error due to the AC Stark shift at the level of 0.1 mrad/kHz corresponding to a sensitivity to this effect reduced by a factor of 50. When running the interferometer, we directly optimize the AC Stark shift on the atomic signal with an accuracy better than 500 Hz, leading to a residual systematic error below 0.05 mrad which is negligible.

3. Two-photon light shift

As explained above the retro-reflected Raman beams couple the ground state $|6S_{1/2}, F = 3, \mathbf{p}\rangle$ with the two states $|6S_{1/2}, F = 4, \mathbf{p} \pm \hbar\mathbf{k}_{\text{eff}}\rangle$. Since these two possible Raman transitions are Doppler shifted, we can choose only one state by adjusting the Raman detuning. However, the non-resonant coupling induces a two-photon light shift (TPLS) on the selected Raman transition which results in an atomic phase shift ($\Delta\Phi_{TPLS}$) [27]:

$$\Delta\Phi_{TPLS} = \frac{\Omega_{\text{eff}}^{(1)}}{4\delta_D^{(1)}} - \frac{\Omega_{\text{eff}}^{(3)}}{4\delta_D^{(3)}} \quad (9)$$

where $\Omega_{\text{eff}}^{(i)}$ is the effective Rabi frequency and $\delta_D^{(i)}$ the Doppler shift for the i^{th} pulse. This phase shift depends on \mathbf{k}_{eff} and cannot be cancelled out with the k-reversal method. It is shown that this shift is similar for the two interferometers and induces an error only on the acceleration signal of 12 mrad and remains below 0.3 mrad on the rotation signal.

4. Wave-front distortion

The atomic phase shift depends on the effective laser phase ϕ_i imprinted on the atomic wave at the moments of the three pulses. Because of a non-uniform laser wave-front, the phase shift measured by the interferometers

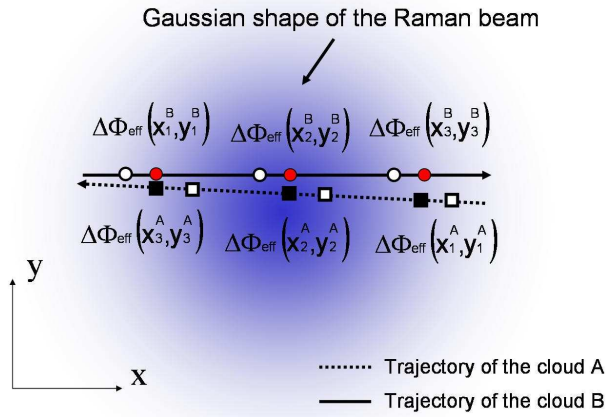


FIG. 11: Wave-front defects induced a phase shift related to the laser phase seen by the atoms at the moment of the three laser pulses (black squares and red dots). By changing the moment when the pulses occurs we simulate a relative displacement of the atomic cloud with respect to the Raman beam (white squares and white dots).

depends on the position of the atomic cloud in the Raman wave-front (x_i, y_i) at the i^{th} pulse and can be written as:

$$\Delta\Phi_{\text{wf}} = \phi_1(x_1, y_1) - 2\phi_2(x_2, y_2) + \phi_3(x_3, y_3) \quad (10)$$

The spatial variations of the laser phase along the wave-front induce a phase shift on the interferometric measurements. In our setup, the use of a retro-reflected configuration allows to reduce the number of optical elements and decrease the aberrations between the two opposite Raman beams. Therefore, the wave-front defects are mainly induced by the Raman window, the quarter wave plate and the retro-reflection mirror which affect only the reflected beam.

When the trajectories of the two atomic clouds are perfectly overlapped, the wave-front defects are identical for both interferometers and then equivalent to a constant acceleration. If the paths are not perfectly overlapped, the phase shifts due to these wave-front defects are not identical and appear as an error on the rotation signal when subtracting the phase shifts of the two interferometers [28]. This is illustrated in Fig. 11 representing the position of the atomic clouds at the time of the three pulses $\pi/2 - \pi - \pi/2$. The error on the rotation signal results from the half difference of the two wave-front distortion phase shift: $\Delta\Phi_{\text{wf}} = \frac{\Delta\Phi_{\text{wf}}^A - \Delta\Phi_{\text{wf}}^B}{2}$.

A first estimation of this effect was performed by measuring the wave-front distortion induced by a single and not mounted Raman windows with a Zygo wave-front analyzer [29]. From these measurements, we deduce a wave-front phase shift of 20 mrad on the rotation signal for an interaction time of $2T = 80$ ms, which is consistent with the error measured on the rotation signal. A second method was implemented to estimate this effect by moving the positions $(x_i, y_i)^{A,B}$ of the atomic clouds in the Raman beam at the moment of the pulses. This can

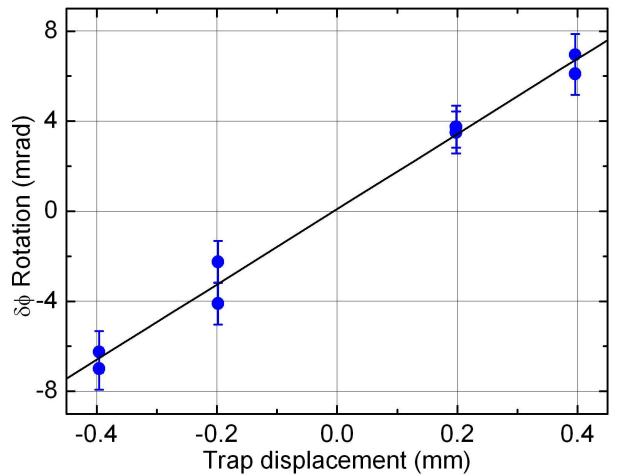


FIG. 12: Rotation phase shift measured as a function of the atomic cloud positions along the x direction. The displacements of the atomic position compared to the laser beam are applied by changing the timing of the laser pulse sequence.

be performed by changing the delay between the launching and the first Raman pulse, keeping the duration of the interferometer constant ($2T = 80$ ms). Consequently, the positions of the two atomic clouds are shifted in opposite directions, as shown on Fig. 11. In the Fig. 12, the rotation phase is displayed as a function of the delay compared to the usual laser sequence, and translated into trajectory shift. For small deviations, the phase shift due to wave-front defects can be linearized. Therefore we infer the sensitivity of the rotation measurement to a relative displacement along the x direction between the two sources by performing a linear fit of the data. The sensitivity obtained is:

$$\frac{\Delta\Phi_{\text{wf}}}{\delta x} = 17 \mu\text{rad}/\mu\text{m} \quad (11)$$

5. Conclusion on systematic errors

We studied the relative contributions of different sources of parasitic phase shifts. The dominant contribution to the systematic effects has been identified as coming from the wave-front distortions. Indeed, an independent evaluation of its contribution (~ 20 mrad) is in agreement with the actual parasitic phase shift (28.3 mrad) for $2T = 80$ ms (Fig. 9(b)). This effect gets significant when the interrogation time exceeds 30 ms. We attribute this to the growth of wave-front distortions on the edge of the windows. Using a larger window or the center of three separated windows for the three pulses would allow to limit its impact.

IV. SENSITIVITY

The bias stability of the acceleration and rotation signals was studied by orienting the area of the interferometer in the East-West direction so that the rotation rate measured is zero. Consequently, it is possible to measure a phase shift by setting the interferometers on the side of the fringe for both interferometers simultaneously. Then we calculate the phase shift from the measured probabilities $P^{A,B}$, the contrast $C^{A,B}$ and the offsets $M^{A,B}$.

Since the interferometers operate at the side of a fringe, the fluctuations of the contrasts parameters $C^{A,B}$ do not impact significantly the measured probability. Consequently, the contrast values are determined once at the beginning of the measurement, by fitting the fringe pattern with a sinusoidal function. To get rid of offset fluctuations, the experimental sequence alternates a measurement on the both sides of the central fringe. The half-difference between two successive measurements yields the atomic phase shift rejecting the offset fluctuations. Moreover, the sign of the effective wave vector \mathbf{k}_{eff} is reversed between two successive steps.

The Fig. 13 shows such record of the two inertial signals as a function of the time, for an interaction time of $2T = 80$ ms and a repetition rate of 1.72 Hz. The large oscillations which appear on the acceleration signal only are due to tidal effects and are removed on the rotation signal illustrating a key feature of our geometry. A more quantitative study of the separation between the acceleration and rotation signal demonstrated a 76 dB rejection rate, the details of this study are presented in the appendix A. The efficiency of this rejection is due to the fact that the wave packets of the two sources interact with the same equi-phase plane of the Raman beams at exactly the same time.

A. Acceleration measurements

The acceleration signal is deduced from the sum of the two interferometer phase shifts. The short term sensitivity obtained on these measurements is $5.5 \times 10^{-7} \text{ m.s}^{-2}.\text{Hz}^{-1/2}$. This sensitivity is mainly limited by the residual vibrations of the platform as for atomic gravimeter [30]. Standard deviation (Fig. 15(a)) of the acceleration signal shows an improvement of the sensitivity as $\tau^{-1/2}$ as expected. By integrating our measurement over 5000 s, we reach a sensitivity of 10^{-8} m.s^{-2} which is close to our atom gravimeter characteristics presented in [30]. The difference between the sensitivity of the two apparatus is explained by slightly smaller repetition rate and interrogation time. In order to reach such a sensitivity, the noise contribution from vibrations is filtered out thanks to a passive isolation platform (nanoK 350BM-1). The residual noise is furthermore reduced by a correlated measurement performed with a low noise seismometer (Guralp T40) [30]. Additionally, variations of the gravity g due to tidal effect are computed from a

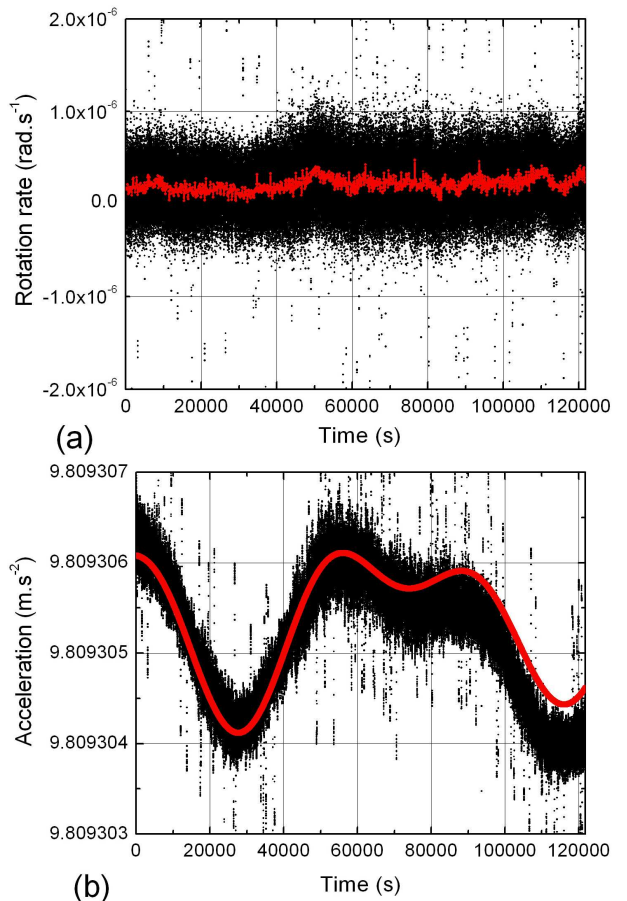


FIG. 13: Rotation (a) and acceleration (b) measurements as a function of the time, obtained for an interaction time of $2T = 80$ ms on a 12 hours continuous acquisition. The rotation data (a) are presented shot-to-shot (black dots) and averaged over 100 s (red line). The shot-to-shot acceleration measurement (b) is compared to expected variations of the gravity (line) due to tidal effect.

model provided by tide parameters extracted from [31] and subtracted from the signal in order to infer the long term stability of the sensor.

B. Noise on the Rotation signal

The rotation phase shift is extracted from the difference between the signals of the two interferometers. The Allan standard deviation is plotted in Fig. 15(b). The short term sensitivity of the rotation signal is $2.4 \times 10^{-7} \text{ rad.s}^{-1}.\text{Hz}^{-1/2}$. The Allan standard deviation decreases with integration time as $\tau^{-1/2}$, down to 1000 seconds, reaching a sensitivity of $10^{-8} \text{ rad.s}^{-1}$.

The Allan standard deviation of the rotation signal at one second is limited by the quantum projection noise evaluated in section II C 2. In order to confirm this point, we perform measurements for different numbers of atoms by changing the loading time of the two MOTs. Assum-

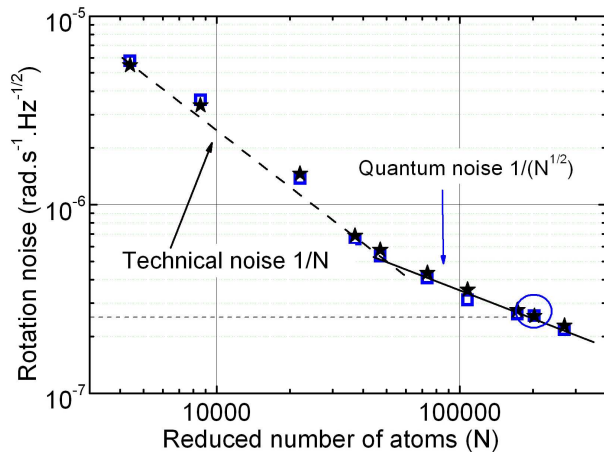


FIG. 14: Rotation noise at 1 second measured on the interferometer (blue circles) and estimated taking into account the parameters of the detection system (stars) as a function of the reduced atom number. The circle shows the usual parameters of the experiment corresponding to a reduced number of 2×10^5 atoms per shot.

ing that the detection noise is independent for the two interferometers A and B, its impact on the standard deviation σ_Φ of the rotation phase shift yields:

$$\sigma_\Phi^2 = \frac{1}{4C^2} \left(2\alpha + \frac{1}{4} \left(\frac{1}{N_A} + \frac{1}{N_B} \right) + \gamma \left(\frac{1}{N_A^2} + \frac{1}{N_B^2} \right) \right) \quad (12)$$

The contrasts of the two interference fringes are identical for the two interferometers, and noted C . The coefficients α and γ are related to the detection features and have been determined in section II C 2. In order to characterize the contribution of the detection noise, it is convenient to plot the rotation phase noise versus the number of atoms. For a given loading time, the number of trapped atoms is different for the two atomic sources A and B, so we define an reduced atom number $N = \frac{N_A N_B}{N_A + N_B}$. Thus the equation (12) becomes:

$$\sigma_\Phi^2 \simeq \frac{1}{4C^2} \left(2\alpha + \frac{1}{4N} + \frac{\gamma}{N^2} \right) \quad (13)$$

In Fig. 14 the rotation noise (blue circles) is displayed versus the reduced atom number. The data correspond to the Allan standard deviation at 1 second of the rotation phase shift calculated from series of 10 minutes measurements. The black stars correspond to the noise estimated from the equation (13) in which the coefficients α, γ were measured independently of the interferometric measurement (section II C 2). We note an excellent agreement between rotation noise measured with the two interferometers and the detection noise evaluated independently. The number of atoms in the usual conditions is rounded in the Fig. 14, which corresponds to a rotation noise of $2.4 \times 10^{-7} \text{ rad.s}^{-1} \cdot \text{Hz}^{-1/2}$, limited by the quantum projection noise. An improvement by a factor of 45 on the atom number ($\sim 10^7$ atoms), would

allow to reach the detection noise plateau independent on the atom number, estimated from the parameter γ at $4 \times 10^{-8} \text{ rad.s}^{-1} \cdot \text{Hz}^{-1/2}$. Such number of atoms is currently obtained during the usual loading time of our interferometer by using a 2D MOT [32].

C. Long term stability

The long term sensitivity achieves a plateau at $10^{-8} \text{ rad.s}^{-1}$ for time scales longer than 1000 s. We have realized a systematic study of all possible sources of drift, which can limit the sensitivity for longer measurement times. First, we have verified that the orientation of the sensitive rotation axis were stable in space. Second, we have quantified the effect of a possible drift from every systematic error source. Only the fluctuations of trajectories, coupled to the wave-front distortions of the Raman laser, can explain the observed drift. The typical position fluctuations ($20 \mu\text{m}$) and drift sensitivity of $10^{-9} \text{ rad.s}^{-1}/\mu\text{m}$ gives a typical limit of the order of $2 \cdot 10^{-8} \text{ rad.s}^{-1}$ in agreement with the observed value.

This main limitation can be reduced drastically by combining an improvement of wave-front of the Raman laser and the reduction of the position fluctuations. Placing the retro-reflection system ($\lambda/4 + \text{mirror}$) inside the vacuum chamber removes aberrations induced by the window, which represents the highest contributions. Stabilities of trajectories can be improved by the use of other kind of optical fibers (better stability of the polarization) or an active stabilization of polarization and intensity of each cooling beam.

V. CONCLUSION

We carried out the characterization of a cold atom gyroscope in term of sensitivity, systematic errors and scale factor, and clearly identified its limits. A study of the scale factor have demonstrated an excellent linearity and stability, limited by the resolution due to the drift of the bias. Its main contribution is related to the fluctuations of the atomic trajectories. When coupled to the Raman wave-front distortions, they also limit the long term stability of the rotation measurements. At short term, the sensitivity was given by the quantum projection noise thanks to the use of a double-interferometer, which allows to perfectly cancel the phase shift due to parasitic vibrations. More generally, similar effects from wave-front distortions should appear on the other kind of dual cold atom interferometers, based on molasses techniques, as in gravity gradiometer [22, 23] or in the test of the universality of free fall by comparing acceleration of two clouds of different species [33, 34].

Finally, these limits are not fundamental and can be overcome by at least one order of magnitude by different improvements. The parasitic shifts due to wave-front distortions can be reduced by improving the quality of the

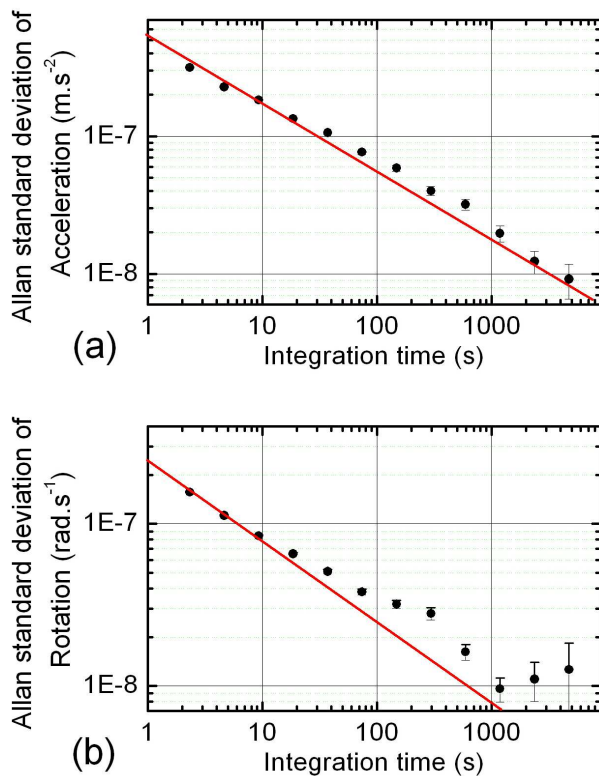


FIG. 15: Allan standard deviation calculated for acceleration (a) and rotation (b) measurements (dots) from a 36 hours continuous acquisition. The lines show the expected improvement of the sensitivity as $\tau^{1/2}$

optics and the stability of the launching velocities. Furthermore, their impact in term of rotation rate can be reduced by modifying the geometry. Indeed, atoms can be launched in more straight trajectories with a higher longitudinal velocity as in Ref. [14] or by using the four pulse configuration previously demonstrated in [11], with longer interaction time. In both cases, the area of the interferometer significantly increased while keeping the phase shift due to wave-front distortion almost constant. Performances at long term should then be improved to reach an expected level below 10^{-10} rad.s $^{-1}$, opening the way to new application fields for atomic gyroscopes.

Acknowledgments

We would like to thank Ch. Bordé, P. Bouyer, A. Claron, N. Dimarcq, J. Fils, D. Holleville, P. Petit, F. Yver-Leduc, who contributed to build the setup in the early stage of the experiment. We also thank F. Pereira Dos Santos for fruitful discussions and careful reading. We thank the Institut Francilien pour la Recherche sur les Atomes Froids (IFRAF) and the European Union (FINAQS STREP/NEST project contract no 012986 and EuroQUASAR/IQS project) for financial support. T.L.

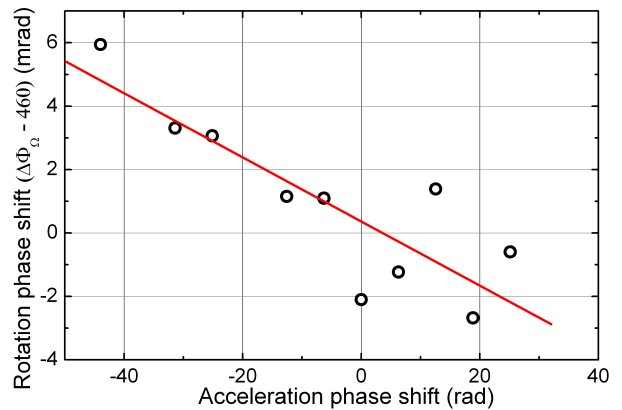


FIG. 16: Measurement of the rotation phase shift as a function of the acceleration induced by varying the inclination of the interferometer plane. The measurements are performed in the horizontal Raman configuration with interferometers of $2T = 60$ ms of total interaction time. Each point corresponds to a measurement achieved for a given angle ε .

thanks the DGA for supporting his work. W.C. thanks IFRAF for supporting his work.

APPENDIX A: SEPARATION OF ACCELERATION AND ROTATION PHASE SHIFTS

As our apparatus measures simultaneously two independent effects (acceleration and rotation), it is crucial to quantify how these two phase shifts are discriminated by the dual interferometer technique. Since the experiment enables to measure the six axis of inertia [11], this characterization has been carried out in the horizontal Raman configuration which enables to easily vary the acceleration phase shift on a large scale and in a controlled way. Best performances, using this configuration, have been presented in Ref. [35] and are summarized in the following section.

1. Horizontal Raman beam configuration

In the horizontal configuration, the retro-reflected Raman beam is orientated in the y direction so as to realize the two interferometers in the (xy) plan at the apex of the trajectories. Therefore the interferometric phase shift is sensitive to the horizontal acceleration a_y and the vertical rotation rate Ω_z . When the Raman beams are perfectly horizontal, the absolute value of the acceleration measured by the interferometer is close to zero while the rotation measurement records the vertical component of the Earth rotation rate $\Omega_z^E = 5.49 \times 10^{-5}$ rad.s $^{-1}$.

This configuration allows inertial measurements with a total interaction time up to $2T = 60$ ms. Data are acquired in a similar way than in the vertical config-

uration, alternating measurements on the two sides of the central fringe, and for two opposite effective wave vectors. The short term sensitivity to the rotation is $5.5 \times 10^{-7} \text{ rad.s}^{-1}.\text{Hz}^{-1/2}$. Performances are similar to the one obtained on the vertical axis, taking in account the shorter interaction time T and reduced contrast (20% instead of 30%).

2. Test of the separation

The horizontal configuration is well adapted to the measurement of the rejection of the acceleration phase shift on the rotation measurement. Indeed, as the interferometer is realized in the horizontal plane, it is possible to induce a large controlled change of the acceleration by tilting the device by an angle of ε with respect to the

horizontal direction. The interferometer then measures a residual component of the gravitation g given by :

$$\Delta\Phi_a = k_{\text{eff}}g \sin \varepsilon T^2 \quad (\text{A1})$$

By tilting the interferometer plan in a range of 0.5 mrad, we change the acceleration phase shift from $\Delta\Phi_a = -45$ to 25 rad. The Fig. 16 displays the rotation phase shift as a function of the acceleration induced on the interferometer. The measurements exhibit a very small slope of 1.5×10^{-4} . The effect of the acceleration on the rotation signal is cancelled at a level better than 76 dB.

This measurement demonstrates the efficiency of a dual interferometer gyroscope for applications in presence of a relatively high level of acceleration noise.

-
- [1] C.M. Will. The confrontation between general relativity and experiment. *Living Reviews in Relativity*, **9**(3) (2006).
- [2] H. Igel, A. Cauchard, J. Wassermann, A. Flaws, U. Schreiber, A. Velikoseltsev, and N.P. Dinh, *Geophys. J. Int.* **168**, 182 (2007).
- [3] A. Lawrence, *Modern Inertial Technology* (Springer, New York, 1998).
- [4] J.F. Clauser, *Physica B* **151**, 262 (1988).
- [5] F. Riehle, Th. Kister, A. Witte, J. Helmcke and Ch.J. Bordé, *Phys. Rev. Lett.* **67**, 177 (1991).
- [6] M. Kasevich and S. Chu, *Phys. Rev. Lett.* **67**, 181 (1991).
- [7] T. L. Gustavson, P. Bouyer, M. A. Kasevich, *Phys. Rev. Lett.* **78**, 2046 (1997).
- [8] A. Lenef, T. D. Hammond, E. T. Smith, M. S. Chapman, R. A. Rubenstein, and D. E. Pritchard, *Phys. Rev. Lett.* **78**, 760 (1997).
- [9] T. L. Gustavson, A. Landragin, M. A. Kasevich, *Class. Quantum Grav.* **17**, 1-14 (2000).
- [10] D. S. Durfee, Y. K. Shaham, and M. A. Kasevich, *Phys. Rev. Lett.* **97**, 240801 (2006).
- [11] B. Canuel, F. Leduc, D. Holleville, A. Gauguet, J. Fils, A. Viridis, A. Clairon, N. Dimarcq, Ch.J. Bordé, A. Landragin, and P. Bouyer, *Phys. Rev. Lett.* **97**, 010402 (2006).
- [12] S. Wu, E. Su, and M. Prentiss, *Phys. Rev. Lett.* **99**, 173201 (2007).
- [13] P. Wang, R.B. Li, H. Yan, J. Wang, and M.S. Zhan, *Chin. Phys. Lett.* **24**, 27 (2007).
- [14] T. Müller, M. Gilowski, M. Zaiser, T. Wendrich, W. Ertmer, and E.M. Rasel, *Eur. Phys. J. D* **53**, 273 (2009).
- [15] Ch. J. Bordé, *Phys. Lett. A* **140**, 10-12 (1989).
- [16] Ch. Antoine, and Ch. J. Bordé, *J. Opt. B: Quantum Semiclass. Opt.* **5**, S199-S207 (2003)
- [17] X. Baillard, A. Gauguet, S. Bize, P. Lemonde, P. Laurent, A. Clairon, and P. Rosenbusch, *Opt. Commun.* **266**, 609 (2006).
- [18] F. Yver-Leduc, P. Cheinet, J. Fils, A. Clairon, N. Dimarcq, D. Holleville, P. Bouyer, and A. Landragin, *J. Opt. B: Quantum and Class. Opt.* **5**, S136-S142 (2003).
- [19] T. Lévêque, W. Chaïbi, A. Gauguet and A. Landragin, *in preparation.*
- [20] G. Santarelli, Ph. Laurent, P. Lemonde, A. Clairon, A.G. Mann, S. Chang, A.N. Luiten, C. Salomon, *Phys. Rev. Lett.* **82**, 4619 (1999).
- [21] W.M. Itano, J.C. Bergquist, J.J. Bollinger, J.M. Gilligan, D.J. Heinzen, F.L. Moore, M.G. Raizen, D.J. Wineland, *Phys. Rev. A* **47**, 3554 (1993).
- [22] J. M. McGuirk, G. T. Foster, J. B. Fixler, M. J. Snadden, and M.A. Kasevich, *Phys. Rev. A* **65**, 033608 (2002).
- [23] G. Lamporesi, A. Bertoldi, L. Cacciapuoti, M. Prevedelli, and G.M. Tino, *Phys. Rev. Lett.* **100**, 050801 (2008).
- [24] Similar results have been observed in a gravimeter experiment [30] while atomic clouds are not launched but only dropped.
- [25] D.S. Weiss, B.C. Young, and S. Chu, *Appl. Phys. B* **59**, 217-253 (1994).
- [26] K. Moler, D.S. Weiss, M. Kasevich, and S. Chu, *Phys. Rev. A* **45**, 342 (1992).
- [27] A. Gauguet, T.E. Mehlstäubler, T. Lévêque, J. Le Gouët, W. Chaïbi, B. Canuel, A. Clairon, F. Pereira Dos Santos and A. Landragin, *Phys. Rev. A* **78**, 043615 (2008).
- [28] J. Fils, F. Leduc, P. Bouyer, D. Holleville, N. Dimarcq, A. Clairon, and A. Landragin, *Eur. Phys. J. D* **36**, 257 (2005).
- [29] J. Fils, PhD thesis, Université Paris XI (2002).
- [30] J. Le Gouët, T.E. Mehlstäubler, J. Kim, S. Merlet, A. Clairon, A. Landragin, and F. Pereira Dos Santos, *Appl. Phys. B* **92**, 133-144 (2008).
- [31] Robertson et al. *Metrologia* **38**, 71 (2001).
- [32] K. Dieckmann, R.J.C. Spreeuw, M. Weidemüller, and J.T.M. Walraven, *Phys. Rev. A* **58**, 3891 (1998).
- [33] R.A. Nyman, G. Varoquaux, F. Lienhart, D. Chambon, S. Boussen, J.-F. Clément, T. Miller, G. Santarelli, F. Pereira Dos Santos, A. Clairon, A. Bresson, A. Landragin, and P. Bouyer, *Appl. Phys. B* **84**, 673681 (2006).
- [34] W. Ertmer *et al.*, *Exp Astron* **23**, 611649 (2009).
- [35] A. Landragin, B. Canuel, A. Gauguet, and P. Tuckey, *Revue Française de Métrologie* **10**, 11-16 (2007).